

<https://doi.org/10.1038/s43247-025-02638-x>

Global coastal water clarity has increased due to human intervention

Check for updates

Fengqin Yan^{1,2,9}, Bin He^{1,3,4,9}, Vincent Lyne⁵, Rong Fan^{1,2}, Yikun Cui⁶, Xinyi Wang^{1,2}, Dongjie Fu^{1,2}, Michael Meadows^{3,7}, John Wilson⁸, Ziying Chen^{1,2}, Chengyuan Ju^{1,3,4} & Fenzen Su^{1,2,3,4} ✉

Climate change and human activity are reshaping coastal systems, yet global impacts on water clarity remain poorly quantified. Here we leverage remote sensing big data to develop a global model of coastal suspended particulate matter across continental coastal waters, and show that global coastal suspended particulate matter concentrations have declined by 0.28 mg L^{-1} annually since 2000, driven by natural processes and human intervention. Furthermore, the spatial extent of areas exceeding the 2000 global mean threshold has shifted landward at an average rate of $0.014 \text{ km year}^{-1}$. Long-term sea level rise and diminished sediment delivery—driven by urbanization and expanding impervious surfaces—were the dominant drivers of this global clarification trend. In contrast, moderate increases in wave height and salinity enhanced resuspension, while larger shifts promoted suspended particulate matter settling. These findings provide a basis for tracking suspended particulate matter trends and guiding sustainable coastal management under urban and climatic pressures.

Global climate change, linked to substantial anthropogenic forcing^{1,2}, has triggered cascading disruptions across Earth's critical coastal interfaces—where 90% of marine biodiversity converges and 40% of humanity resides. As emphasized by the IPCC Sixth Assessment Report³, this rapid acceleration of climatic forcing has intensified terrestrial-oceanic couplings beyond historical analogs. However, the underlying processes governing these interactions remain poorly understood. Accelerated ice-sheet meltwater⁴ and intensified hydro-meteorological extremes^{5,6} have disrupted sediment delivery systems that stabilized nearshore ecosystems over millennial timescales^{7–9}. Concurrently, rising sea levels and altered wind regimes^{10,11} are intensifying coastal erosion and wave-driven sediment remobilization. Together with expanding coastal urbanization^{12,13} these perturbations are reconfiguring sediment transport pathways and driving emergent degraded water quality hotspots characterized by suspended particulate matter (SPM) accumulation. Crucially, the nonlinear couplings between climate-driven hydrodynamic shifts¹⁴ and anthropogenic pressures on nearshore environments^{15,16} generate feedbacks that may exceed biogeochemical thresholds for coastal water clarity—a vital indicator of ecosystem health. These synergistic forces create intricate and spatially divergent patterns of material flux between land and sea, with some coastal

regions experiencing sediment depletion while others exhibit localized accumulation or enhanced resuspension. Such heterogeneity underscores the need to better understand the long-term trends and multifactorial drivers shaping land–ocean exchanges.

Advances in remote sensing big data have transformed the monitoring of land–ocean interactions, providing high spatial and temporal resolution and deep insights into these dynamic exchanges. While agencies like the U.S. Environmental Protection Agency emphasize SPM as a key water quality metric, their understanding of how these fluxes respond to the combined pressures of human activities and climate change on a global scale remains limited. Satellite-derived data products, such as those tracking sediment transport, ocean currents, and land–ocean flux estimates, are indispensable for deepening our understanding of these interconnected systems. Despite advances in satellite-based coastal monitoring^{17,18}, critical knowledge gaps persist in deciphering how these multiscale drivers synergistically govern global patterns of water clarity. The absence of a unified framework to reconcile localized sediment dynamics with planetary-scale transport mechanisms hinders predictive understanding of coastal ecosystem resilience, particularly in quantifying the relative contributions of climate forcing versus anthropogenic pressures on SPM budgets.

¹State Key Laboratory of Resources and Environmental Information System, Institute of Geographic Sciences and Natural Resources Research, Chinese Academy of Sciences, Beijing, China. ²College of Resources and Environment, University of Chinese Academy of Sciences, Beijing, China. ³School of Geography and Ocean Science, Nanjing University, Nanjing, China. ⁴Collaborative Innovation Center of South China Sea Studies, Nanjing University, Nanjing, China. ⁵IMAS-Hobart, University of Tasmania, Hobart, TAS, Australia. ⁶Department of Resources and Environmental Sciences, Quanzhou Normal University, Quanzhou, Fujian, China. ⁷Environmental & Geographical Science Building, University of Cape Town, Cape Town, South Africa. ⁸College of Letters, Arts and Sciences, University of Southern California, Los Angeles, CA, USA. ⁹These authors contributed equally: Fengqin Yan, Bin He. ✉e-mail: sufz@reis.ac.cn

We focused on the 100 km marine ecotone along continental coastlines worldwide, leveraging 23 years (2000–2023) of consistent moderate resolution imaging spectroradiometer (MODIS) observations to track decadal-scale trends in coastal SPM, decode multiscale land–ocean coupling mechanisms, and assess their anthropogenic and climatic drivers. A remote sensing dataset for coastal suspended sediment concentration was developed to analyze spatiotemporal patterns of global coastal SPM levels, derived from the National Aeronautics and Space Administration (NASA)'s Terra and Aqua MODIS satellites' global daily land surface reflectance (SR) products (500-m resolution). A coastal SPM retrieval algorithm, adapted from a global reference method¹⁸, was systematically implemented. Validation against in-situ SPM measurements from 1106 coastal observatories confirmed methodological robustness, demonstrating a median absolute percentage error (MAPE) of 21.1% across global heterogeneous marine environments. Our methodology quantifies coastal waters SPM transport using impervious surface area (ISA)¹⁹ as the human pressure index, while integrating sea surface height (SSH), wave height, and salinity as natural drivers. The analytical framework is grounded in established sediment transport models^{20–22} but innovates through global-scale big data spatio-temporal coverage and machine learning-enhanced pattern recognition.

Global patterns of coastal waters

Regions with an annual mean SPM concentration exceeding 10 mg L^{-1} accounted for ~28% of the global continental coastal waters. High SPM concentrations were primarily observed in high-latitude coastal zones, with annual means surpassing 50 mg L^{-1} in several estuaries and their adjacent waters (Fig. 1a). Among the top 20 countries ranked by the proportion of coastal waters (within 100 km) with annual mean SPM concentrations exceeding 10 mg L^{-1} , most are developing or emerging economies. Belgium, Finland, United States, Estonia, Canada, and United Kingdom are notably the only developed countries appearing on this list (such as Supplementary Fig. 7).

Generally, SPM concentrations exhibited a gradual decline over the period 2000–2023. The distributions of model-predicted annual mean SPM for the years 2000, 2008, 2016, and 2023 (Fig. 1b) show a progressive shift toward lower concentration values, indicating a consistent decrease in sediment levels across global continental coastal waters over the past two decades. Significant declines were observed in specific coastal regions, including Liaodong Bay (China), Port Hedland (Australia), the northern Amazon River plume (Brazil), and Gironde Estuary (France) (such as Supplementary Fig. 8). The spatial extent of high SPM concentrations has

progressively retreated landward over the past two decades, indicating a contraction of turbid zones toward the coastline.

Decline and landward retreat of coastal SPM

To better characterize regional variability, trends in SPM across global coastal waters from 2000 to 2023 were classified into five categories: Further Clearing, Gradually Clearing, Steady, Gradually Turbifying, and Further Turbifying (Fig. 2). Although the Further Clearing category comprises ~16% of total coastal pixels, it alone accounted for more than 66% of the global declining trend in SPM concentrations. The Gradually Clearing region contributed an additional 4.5%, and together these two categories explain over 70% of the global SPM decline (Fig. 2c), highlighting the dominant influence of strong clearing zones in shaping global trends.

Using the global annual mean SPM concentration in 2000 as a reference threshold, we found that areas exceeding this baseline have progressively retreated landward over the past 23 years, with an average recession rate of approximately $0.014 \text{ km year}^{-1}$ (Fig. 2b). This suggests that clearer waters are extending toward the shoreline in many regions, while turbid zones are shrinking. Regionally, coastal waters in mid and low latitude zones exhibited the most pronounced SPM declines between 2000 and 2023, with the Australian coastline alone contributing over 30 percent to the global downward trend (Fig. 2a). Over the same period, SPM concentrations have decreased at an average rate of 0.28 mg L^{-1} per year. In Asia, four major river mouths and delta regions, including the Ganges Brahmaputra Delta in Bangladesh, the Mekong Delta in Vietnam, the Yangtze Estuary in China, and the Yellow River Estuary in China also showed substantial clearing signals, with clearing trends exceeding turbidifying. Notably, Chinese coastal waters exhibited one of the fastest rates of SPM decline globally, alongside Singapore, making both regions key hotspots of rapid coastal sediment reduction and shoreline retreat (such as Supplementary Fig. 9).

Anthropogenic and climatic drivers

To assess the influence of human activities on coastal SPM dynamics, we incorporated global coastal ISA data to distinguish between natural, engineered, and transitioning coastlines. In 2000, coastal regions adjacent to ISA exhibited SPM concentrations that were $\sim 9.64 \text{ mg L}^{-1}$ lower than those in non-ISA regions, suggesting that urbanization and industrial development may be directly associated with reduced SPM levels. From 2000 to 2023, SPM concentrations declined across all coastline types (Fig. 3a). Natural and engineered coastlines exhibited nearly identical rates of decline, with slopes of $-0.1958 \text{ mg L}^{-1} \text{ year}^{-1}$ and $-0.1987 \text{ mg L}^{-1} \text{ year}^{-1}$, respectively. In



Fig. 1 | Global continental coastal waters patterns 2000–2023. a Spatial distribution of the average annual SPM concentration in global continental coastal waters, calculated as the mean of yearly values from 2000 to 2023. **b** Distributions of annual mean SPM concentrations in global continental coastal waters (within 100 km of the coastline) for the years 2000, 2008, 2016, and 2023. Each violin–box

hybrid shows the full data density (shaded area) and summary statistics per year. Boxes represent the interquartile range (25th–75th percentiles), with the horizontal line indicating the median; whiskers extend to the 5th and 95th percentiles. Red dashed lines indicate the annual mean SPM concentration for each year. Sample size for each year is approximately $n \approx 856,000$ valid 0.05° grid cells.

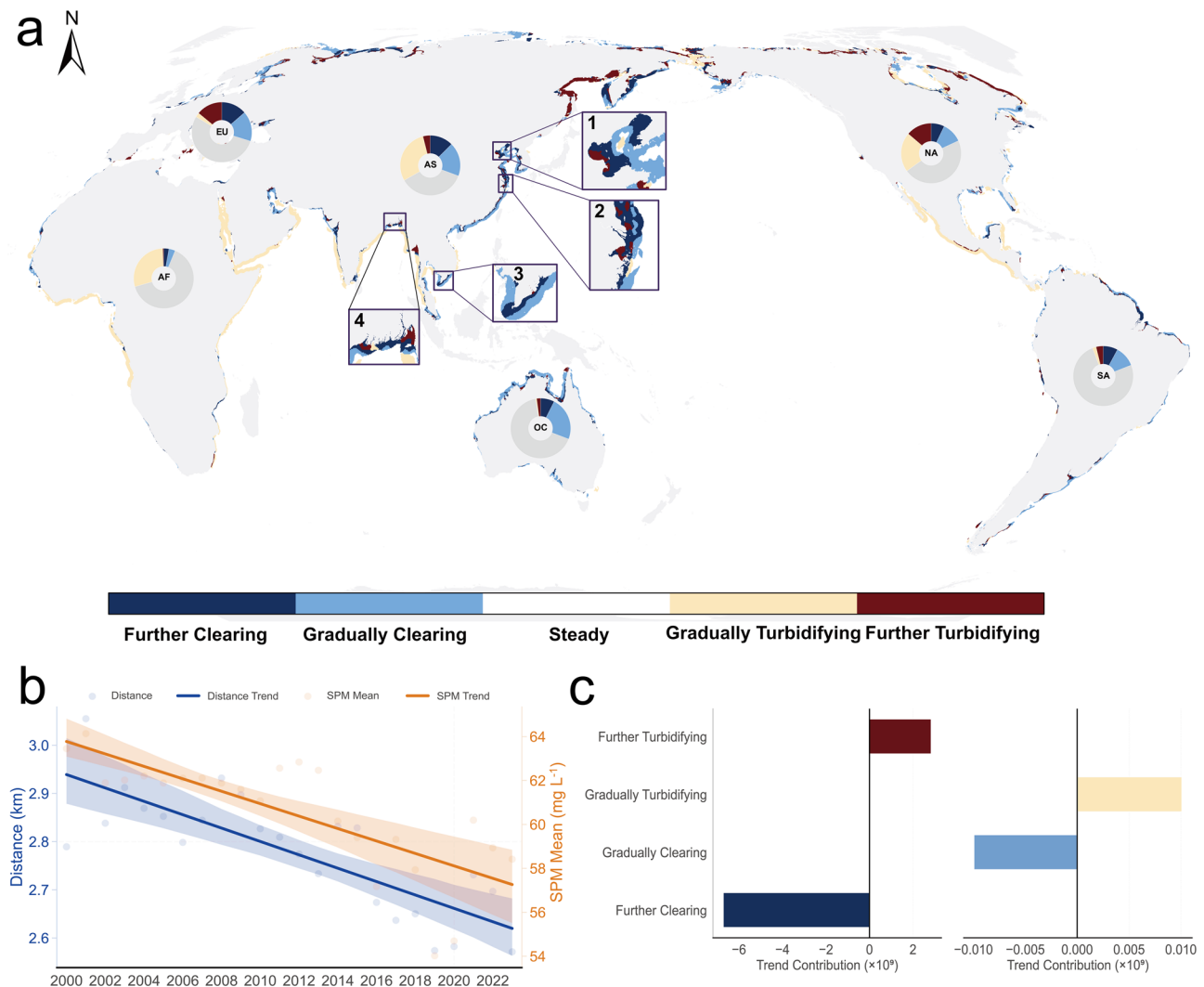


Fig. 2 | Trends and patterns of global continental coastal waters from 2000 to 2023. a Spatial classification of SPM trends in global continental coastal waters based on model-derived annual mean concentrations from 2000 to 2023. Trends are categorized into five classes: Further Clearing (dark blue), Gradually Clearing (light blue), Steady (white), Gradually Turbiding (light orange), and Further Turbiding (dark red). Pie charts indicate the proportional distribution of each trend class by continent: NA (North America), SA (South America), EU (Europe), AF (Africa), AS (Asia), and OC (Oceania). Insets (outlined in dark purple) highlight four representative river mouths and delta systems in Asia: (1) the Yellow River Estuary in China, (2) the Yangtze Estuary in China, (3) the Mekong Delta in Vietnam, and (4)

the Ganges-Brahmaputra Delta in Bangladesh. **b** Temporal change in the average distance between the coastline and the spatial boundary where SPM concentrations match the 2000 global mean. Blue line shows the inland retreat of turbid waters; the orange line shows the declining trend in global annual mean SPM concentrations. Shaded bands represent 95% confidence intervals. Both trends are statistically significant ($P < 0.01$). **c** Contribution of each trend class to the global change in coastal SPM concentrations. Negative values indicate decreasing SPM (clearing), while positive values indicate increasing SPM (turbidifying). Contributions are calculated as the product of slope magnitude, pixel count, and mean concentration.

contrast, coastlines transitioning from natural to engineered conditions showed a less steep decline, potentially reflecting a lag in the response of SPM dynamics to land use change.

Slopes of SSH, wave height, and salinity on coastal SPM trends between 2000 and 2023 show nonlinear response patterns across these variables (Fig. 3b, c). The Shapley Additive exPlanations (SHAP) dependence plots reveal how each variable contributes to the predicted SPM trend. For the SSH slope, SHAP values exhibit an enhanced decline beyond approximately a critical level (~ 0.003), suggesting that rising SSH consistently suppresses SPM levels. In contrast, the salinity slope shows a unimodal response, SHAP values peak between -0.05 and $+0.05$ and decline outside this range. For wave height slope, SHAP values increase within the range of approximately -0.01 to -0.002 , drop near zero, and then stabilize or rise slightly, suggesting that moderate wave energy may enhance SPM while very low or high wave intensities are associated with more stable or decreasing trends.

Discussion

This study provides a comprehensive analysis of global trends in coastal waters sediment transport, focusing on the key natural and anthropogenic factors driving changes in coastal waters over the past 24 years. Utilizing a global-scale remote sensing dataset and an enhanced machine learning retrieval model, we quantified the spatiotemporal patterns of SPM over 2000–2023 as a proxy for sediment dynamics in global continental coastal waters, with selected regional examples used to illustrate key trends. Our findings reveal sustained declines in SPM concentrations across global continental coastal waters over the past two decades, reflecting shifts in coastal sediment dynamics in response to both anthropogenic pressures and climatic variability.

The anthropogenic driver of SPM concentrations was represented by coastal ISA and natural factors comprised: SSH, wave height, and salinity. Both ISA and rising SSH were positively associated with long-term declines

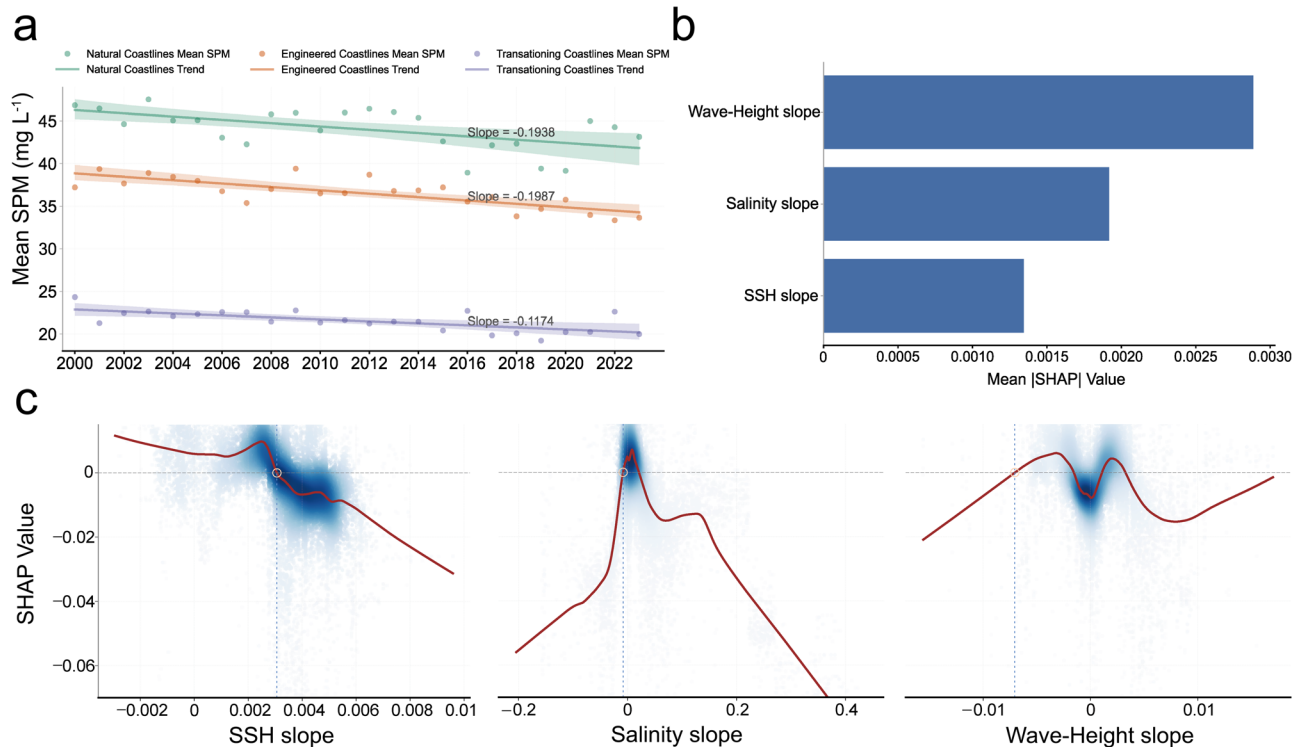


Fig. 3 | Influence of anthropogenic and natural factors on coastal SPM trends from 2000 to 2023. a Temporal trends in annual mean SPM concentrations (2000–2023) across natural coastlines, engineered coastlines, and transitioning coastlines. Coastline types were classified using ISA data. **b** Mean SHAP values indicating the relative importance of physical drivers (SSH slope, salinity slope, and

wave height slope) on SPM trend predictions. **c** SHAP dependence plots showing the nonlinear effects of SSH slope, salinity slope, and wave height slope on SPM slope. Red lines indicate smoothed trends; vertical dashed lines represent SHAP turning points or thresholds.

in SPM concentrations, whereas wave height and salinity exhibit nonlinear relationships, with a mid-range peak, with SPM (Fig. 3).

At the global scale, there was a clear decline in SPM levels over time, particularly in regions where human activities, such as urbanization and industrial development, have led to a significant increase in coastal ISA. Coastal urbanization, particularly in rapidly developing regions such as China, has disrupted land–sea sediment pathways and diminished SPM concentrations in adjacent waters^{23–25}. In areas without significant ISA influence, observed declines in SPM may be associated with the gradual and potentially accelerating SSH (Fig. 3). As water depth increases, vertical mixing and resuspension processes are altered, which typically reduces sediment suspension in offshore waters through enhanced sediment settling^{26,27}. These changes suggest a transition toward sediment-starved coastal systems, especially in urbanized or engineered shorelines.

At the regional scale, several major river mouths and delta systems exhibited pronounced reductions in SPM export to adjacent coastal waters. Notably, four prominent systems in Asia—the Ganges-Brahmaputra Delta (Bangladesh), Mekong Delta (Vietnam), Yangtze Estuary (China), and Yellow River Estuary (China)—showed substantial declines, with the most significant reduction observed in the Yellow River Estuary (Fig. 2a). This reduction in sediment delivery from land to sea is likely attributable to the construction of hydraulic engineering structures such as dams and reservoirs, which have been shown to reduce particulate load by nearly 50%^{28–30}. These findings underscore the role of anthropogenic modifications to river systems in altering coastal sediment dynamics. The complex and nonlinear nature of these interactions highlights the need for further investigation into localized sediment transport processes in highly regulated deltaic regions.

Monotonic declines in SHAP values with increasing SSH slope indicate that long-term sea level rise has a sustained positive contribution in declining SPM concentrations. This pattern may reflect the physical suppression of sediment transport caused by deeper water depths, reduced land–sea gradient, diminished estuarine outflow, or weaker near-bed

turbulence and sediment resuspension as water depth increases. The lack of nonlinearity in the SSH response implies that its influence acts as a gradual yet persistent, and potentially accelerating, forcing mechanism on sediment dynamics.

In contrast, nonlinear SHAP patterns for salinity and wave-height slope point to more complex and threshold-sensitive optimal feedbacks. Salinity changes near zero slope—indicative of stable or low-gradient conditions—may enhance sediment resuspension or inhibit flocculation, leading to increased SPM concentrations. However, larger positive or negative shifts in salinity slope are likely associated with density stratification or reduced turbulence, resulting in greater sediment settling and lower SPM levels. A similar threshold response is evident for wave-height slope: moderate increases tend to promote sediment resuspension, but beyond a certain intensity, stronger wave regimes may drive offshore transport or vertical dilution of sediments, ultimately limiting SPM accumulation. These nonlinear dynamics highlight the dual roles of salinity and wave forcing in both mobilizing and redistributing sediments within coastal waters.

While this study primarily focused on ISA within 5 × 5 km coastal grids and a 5 km landward buffer to assess the localized impacts of shoreline urbanization, additional factors may influence suspended sediment dynamics. Other anthropogenic activities, such as offshore wind farms and oil and gas platforms, can affect SPM levels in certain regions, notably in areas like the northern Yangtze River estuary³¹. Natural drivers, including wind direction and ocean currents, may also shape localized trends, particularly in enclosed bays^{32–34}. Furthermore, broader terrestrial factors such as deforestation, agricultural intensification, and the construction of reservoirs can significantly alter sediment fluxes from inland watersheds, although these factors were beyond the spatial scope of our nearshore-focused framework^{35–38}. Future work should integrate catchment-scale land use and hydrological connectivity to better capture the full continuum of land and ocean sediment interactions in coastal systems.

By integrating remote sensing observations with systematic analysis of physical and socioeconomic drivers, this study establishes a scalable framework for tracking sediment transport trends under global change, highlighting the key drivers and processes that influence coastal water clarity (Fig. 4). The observed shorelineward shift in regions of high SPM, averaging $0.014 \text{ km year}^{-1}$, reflects the dynamic reorganization of coastal sediment regimes at both global and regional scales. This study primarily focuses on coastal drivers, including long-term sea level rise, increasing coastal ISA, and changing salinity and wave height conditions, which collectively reshape SPM dynamics. We also acknowledge that upstream alterations, such as reductions in river discharge and sediment trapping by dams, may exert substantial influence on coastal SPM trends. Although these riverine factors were beyond the scope of our analysis, the observed patterns underscore the combined roles of climatic and anthropogenic pressures in modulating nearshore sediment behavior, with implications for turbidity, nutrient cycling, and ecological stability.

These findings advance understanding of how anthropogenic pressures and climate variability reshape sediment fluxes at the land–sea interface. Recognizing the nonlinear and spatially heterogeneous nature of these dynamics is critical for informing adaptive coastal management. As sediment-starved conditions become more widespread, integrated monitoring frameworks—combining satellite observations, in-situ data, and land-use models—will be essential for sustaining ecosystem resilience. Future progress will depend on the synthesis of multi-scale big datasets and scalable analytical approaches to support locally tailored, evidence-based responses to accelerating climate change and intensifying human impacts.

Methods

Data sources

We utilized daily surface reflectance (SR) products from MODIS Terra (MOD09GA) and Aqua (MYD09GA), with a spatial resolution of 500 m, to estimate SPM. Atmospheric correction and cloud removal were performed on MOD09GA and MYD09GA data using Google Earth Engine (GEE) tools (https://developers.google.com/earth-engine/datasets/catalog/MODIS_061_MOD09GA; https://developers.google.com/earth-engine/datasets/catalog/MODIS_061_MYD09GA#description). These datasets encompass surface spectral reflectance across MODIS bands 1–7, corrected for Rayleigh

scattering, as well as gas and aerosol signals. Residual errors were mitigated through band subtraction, and SR values were further adjusted to the SR_{land} scale to minimize inaccuracies from excessive atmospheric correction in coastal regions³⁹. To reduce the influence of short-term extreme events and episodic anomalies in SPM, we based our analysis on annual mean SPM values computed from GEE-derived cloud-free surface reflectance composites. These annual averages inherently smooth over daily and seasonal variability, including spikes caused by storms, monsoons, or tidal resuspension. Additionally, GEE employs standardized cloud and shadow masking algorithms, ensuring that reflectance data used in model prediction is largely unaffected by persistent cloud cover. Using these corrected SR_{land} datasets, we then developed a global SPM inversion model by matching the remote sensing data to field-measured observations.

We used four databases from in situ field observations: the China Coast and Estuary database (including the Yellow River Estuary, Yangtze River Estuary, Pearl River Estuary); the Sea-Viewing Wide Field-of-View Sensor (SeaWiFS) Bio-optical Archive and Storage System (SeaBASS); and the United Nations Environment Programme Global Environment Monitoring System (GEMStat) (such as Supplementary Fig. 1). These databases cover coastal areas, estuaries, and bays, representing a wide range of turbidity and nutrient conditions, which enabled a thorough assessment and validation of the retrieval algorithm's accuracy. A total of 48 observation points along the coast and estuaries of China from 2001 to 2021 were selected, with SPM concentrations ranging from 2 to 1890 mg L^{-1} . For SeaWiFS, SeaBASS, and GEMStat, 15 coastal areas and 7 estuaries were chosen, with sampling concentrations ranging from 0.0001 to $1740.45 \text{ mg L}^{-1}$. In total, 1106 stations globally were matched with MODIS daily products using GEE.

We utilized the 30-m time-series global ISA (Version 2.0) dataset, which maps annual increases in global ISA from 1972 to 2019¹⁹. This dataset serves as a crucial indicator of urbanization and is used to characterize the scale of impact of human activities along coastlines. We defined coastal ISA as impervious surface coverage exceeding 10% within $5 \times 5 \text{ km}$ coastal grid cells and analyzed their influence within a 5 km landward buffer zone. While we focused on shoreline-adjacent areas, we acknowledge that broader terrestrial drivers such as land clearing and agriculture may also influence sediment dynamics but are beyond the spatial resolution of this framework. For detailed processing methods, please refer to the Supplementary Materials.

As detailed in Table 1, we selected several global environmental reanalysis datasets, including: Wave height, SSH, Salinity, EEZ, and Global coastline.

For the global study area, we selected the Marine Regions' continents dataset based on previous research⁴⁰ and defined the study area as the global continental coastal waters, extending approximately 100 km seaward from the shoreline to match the spatial coverage of MODIS land products and previous coastal studies (such as Supplementary Fig. 1)⁴⁰.

Global coastal waters SPM retrieval algorithm

Following methodology established previously¹⁸, the XGBoost model was used to estimate global SPM. XGBoost incorporates regularized boosting of gradient-based decision trees, which helps reduce model variance⁴¹. The “XGboost” package in Python was used to train the model.

Four bands from the atmospherically corrected MODIS data ($SR_{land}(469)$, $SR_{land}(555)$, $SR_{land}(645)$, $SR_{land}(859)$) were selected as optimal bands for estimating SPM (P_{SPM}). Latitude and longitude were included

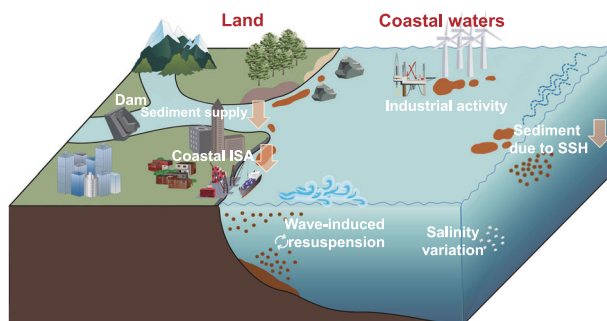


Fig. 4 | Diagram illustrating the main anthropogenic and natural drivers affecting coastal suspended sediment dynamics. Land-based influences include sediment supply from upstream dams and coastal ISA. Oceanic factors include SSH, wave-induced resuspension, salinity changes, and offshore industrial activities. Light orange arrows indicate pathways associated with sediment reduction.

Table 1 | List of datasets used in the study along with their source and link

Dataset	Source	Link
Wave height	Copernicus	https://cds.climate.copernicus.eu/datasets/reanalysis-era5-single-levels?tab=download
SSH	Copernicus	https://data.marine.copernicus.eu/product/GLOBAL_MULTIYEAR_PHY_ENS_001_031/download
Salinity	Copernicus	https://data.marine.copernicus.eu/product/GLOBAL_MULTIYEAR_PHY_001_030/download
EEZ, World Map and Global Coastline	Marine Regions	https://www.marineregions.org/downloads.php

to reduce errors from spatial heterogeneity in the estimation as follows:

$$P_{SPM} = \text{XGboost}(\text{SR}_{\text{land}}(469), \text{SR}_{\text{land}}(555), \text{SR}_{\text{land}}(645), \text{SR}_{\text{land}}(859), \text{SR}_{\text{land}}(859)/\text{SR}_{\text{land}}(645), \text{SR}_{\text{land}}(645)/\text{SR}_{\text{land}}(555), \text{Latitude}, \text{Longitude}) \quad (1)$$

Here, the ratios $\text{SR}_{\text{land}}(859)/\text{SR}_{\text{land}}(645)$ and $\text{SR}_{\text{land}}(645)/\text{SR}_{\text{land}}(555)$ represent two effective band ratios previously used for estimating SPM in certain water bodies^{42–45}. The SWIR bands were not used due to their low signal-to-noise ratios and negligible water-leaving signal at these wavelengths⁴⁶. The model requires the adjustment of several hyperparameters during training, including the type of booster, learning rate, maximum depth, and regularization coefficients.

To accommodate the skewed distribution of SPM concentrations in the training data, we first applied a logarithmic transformation to reduce heteroscedasticity and improve model stability. We then constructed two separate models—one for high SPM and one for low SPM conditions. These models are dynamically selected based on an adaptive threshold and blended through a smooth transition zone to minimize blocky artifacts during prediction.

To evaluate model accuracy, we use the mean absolute error (MAE) (Eq. 2) and MAPE (Eq. 3). MAE values are calculated numerically and expressed as relative differences (i.e., as percentages). Generally, relative differences such as MAPE within ~35% are considered satisfactory for assessing estimation performance relative to measured values, while MAPE > 60% indicates unsatisfactory performance. Refer to the Supplementary Materials for details.

$$\text{MAE} = \left| 10 \frac{\sum_{i=1}^N |\log_{10}(y_i) - \log_{10}(x_i)|}{N} - 1 \right| \times 100\% \quad (2)$$

$$\text{MAPE} = 100\% \times \text{median} \left[\frac{|y_i - x_i|}{x_i} \right] \text{ for } i = 1, 2, \dots, N \quad (3)$$

Global coastal waters SPM trends

To calculate trends for SPM values in the coastal waters of the study area for the period 2000–2023, a linear regression model was used to estimate the annual mean trend for each grid cell, using a spatial resolution of 0.05° (~5 km at the equator), as shown in Eq. (4):

$$y(t) = k_1 t + a_1 \quad (4)$$

where $y(t)$ is the value of the SPM trend, which is a function of time, t (i.e., year), coefficients k_1 and a_1 were determined by standard least-squares approaches.

To extract decadal SPM trends, we removed temporal autocorrelation, computed linear slopes from annual model outputs (2000–2023), excluded extreme outliers, interpolated missing values, and aggregated results to 0.05° resolution for global coastal analysis. To identify significant trends, we employed the Mann–Kendall (MK) test, a widely used non-parametric method for detecting trends and assessing randomness in time series data. All analyses were performed using Python.

Distance from coastline

We quantified the distance of SPM concentrations from the coastline by calculating the spatial shift of a specific concentration level relative to the coast. First, the annual mean SPM concentration for the year 2000 was chosen as the baseline. We then counted the number of grid cells corresponding to this concentration extending from the coastline and determined the total area ($S(i)_{2000\text{mean}}$). The length of the coastline associated with this baseline concentration ($d(i)_{2000\text{mean}}$) was also measured. Finally, we calculated the relative distance of the SPM concentration, as shown in

Eq. (5):

$$D_i = \frac{S(i)_{2000\text{mean}}}{d(i)_{2000\text{mean}}} \quad (i = 2000, 2001, \dots, 2023) \quad (5)$$

In the above equation, i represents the year, and D_i denotes the offshore distance in a given coastal waters area relative to the annual mean SPM concentration for 2000 for year i . For further details, please refer to the Supplementary Materials.

Trend contribution analysis

To quantify the contribution of different regions or trend classes to the overall global change in SPM, we calculated a trend contribution score by weighting the slope of each grid cell by its spatial extent and SPM magnitude. This approach considers both the direction and magnitude of change, as well as the ecological significance of the SPM baseline. For a given grid cell i , its contribution to the global SPM trend is defined as shown in Eq. (6):

$$C_i = S_i \times A_i \times \overline{SPM}_i \quad (6)$$

where C_i is the weighted contribution of grid cell i to the global trend. S_i is the annual SPM trend (slope) at grid cell i , in units of $\text{mg L}^{-1} \text{ year}^{-1}$. A_i is the area of the grid cell (pixel count). \overline{SPM}_i is the mean SPM concentration over the study period at grid cell i , in mg L^{-1} .

The total contribution of a given class or region (e.g., Class 1: further clearing) is calculated as shown in Eq. (7):

$$C_{\text{class}} = \sum_{i \in \text{class}} C_i \quad (7)$$

To estimate the relative contribution (%) of each class or region to the total global trend, we use the method shown in Eq. (8):

$$\text{Contribution} = \frac{|C_{\text{class}}|}{\sum_k |C_k|} \times 100\% \quad (8)$$

where k is the summation over all classes or regions. The absolute value is taken to reflect the relative weight of trend magnitude, regardless of direction. This formulation allows the identification of regions that disproportionately drive global trends due to their strong SPM gradients or high baseline concentrations, even if their spatial extent is limited.

XGBoost and interpretability

We employed the robust and widely used XGBoost Regression model to relate variations in SPM concentrations to the primary drivers of these changes. This machine-learning approach is well-suited for handling long-term, multi-scale datasets with complex structures and multiple predictors.

The model identified strong relationships between coastal SPM concentrations and key environmental drivers, including wave height, SSH, and salinity. To improve the interpretability of each variable's contribution, we employed Shapley Additive exPlanations (SHAP)⁴⁷, a game-theoretic method that assigns optimal contribution scores to individual predictors based on classical Shapley values. To minimize the influence of extreme outliers while preserving dominant trend patterns, we restricted the SHAP analysis to the 5th–95th percentile range of SPM slope values. This filtering step excluded rare and potentially noisy extremes, enabling a more robust focus on core transition regimes—particularly those corresponding to Further Clearing and Further Turbidity trends.

To interpret model outputs, we used SHAP bar plots to quantify the relative contributions of wave height, sea level, and salinity to annual mean SPM concentrations. Trend lines were overlaid to illustrate the direction and form of each relationship, indicating whether variables exerted positive or negative effects on SPM. All modeling and interpretation were performed in Python, using the XGBoost package for training and the SHAP package for post hoc variable attribution.

Data availability

All observations and data supporting the findings of this study were retrieved as follows: Publicly available data on coastal waters sediment measurements were obtained from the SeaWiFS (<https://eosps.nasa.gov/content/nasa-earth-science-data>), SeaBASS (<https://seabass.gsfc.nasa.gov/>), and GEMStat (<https://gemstat.bafg.de/applications/public.html?publicUser=PublicUser#gemstat/Stations>) databases. MODIS data were obtained from the GEE platform (https://developers.google.com/earth-engine/datasets/catalog/MODIS_061_MOD09GA; https://developers.google.com/earth-engine/datasets/catalog/MODIS_061_MYD09GA#description). Global environmental reanalysis datasets, including wave data (<https://cds.climate.copernicus.eu/cdsapp#!/dataset/reanalysis-era5-single-levels?tab=form>), SSH data (https://data.marine.copernicus.eu/product/GLOBAL_MULTIYEAR_PHY_ENS_001_031/download) and salinity data (https://data.marine.copernicus.eu/product/GLOBAL_MULTIYEAR_PHY_001_030/download). EEZ, World Map and Global Coastlines data from Marine Regions Agency (<https://www.marineregions.org/downloads.php>). The continents dataset was from previous research⁴⁰. Global datasets, including annual mean suspended particulate matter (SPM) concentration, shoreline recession distance, and category-wise contributions to SPM trends, are available and can be accessed at: <https://doi.org/10.6084/m9.figshare.29581982.v1>⁴⁸.

Code availability

All analysis code used in this study is available in a public repository at Figshare: <https://doi.org/10.6084/m9.figshare.29589383.v1>.

Received: 25 March 2025; Accepted: 25 July 2025;

Published online: 07 August 2025

References

- Lenton, T. M. et al. Quantifying the human cost of global warming. *Nat. Sustain.* **6**, 1237–1247 (2023).
- Zeebe, R. E., Ridgwell, A. & Zachos, J. C. Anthropogenic carbon release rate unprecedented during the past 66 million years. *Nat. Geosci.* **9**, 325–329 (2016). 2016 9:4.
- Meyer, A., Holbrook, N., Strutton, P. & Eccleston, R. The Intergovernmental Panel on Climate Change (IPCC) Sixth Assessment Report: What does it mean for Tasmania? A special briefing by the Australian Research Council Centre of Excellence for Climate Extremes and the University of Tasmania. (2021).
- Golledge, N. R. et al. Global environmental consequences of twenty-first-century ice-sheet melt. *Nature* **566**, 65–72 (2019).
- Peterson, B. J. et al. Increasing river discharge to the Arctic Ocean. *Science (1979)* **298**, 2171–2173 (2002).
- Milly, P. C. D. & Dunne, K. A. Colorado River flow dwindles as warming-driven loss of reflective snow energizes evaporation. *Science (1979)* **367**, 1252–1255 (2020).
- Hoefel, F. & Elgar, S. Wave-induced sediment transport and sandbar migration. *Science (1979)* **299**, 1885–1887 (2003).
- Vercruysse, K., Grabowski, R. C. & Rickson, R. J. Suspended sediment transport dynamics in rivers: multi-scale drivers of temporal variation. *Earth Sci. Rev.* **166**, 38–52 (2017).
- Toimil, A. et al. Climate change-driven coastal erosion modelling in temperate sandy beaches: Methods and uncertainty treatment. *Earth Sci. Rev.* **202**, 103110 (2020).
- Burger, F. A., Terhaar, J. & Frölicher, T. L. Compound marine heatwaves and ocean acidity extremes. *Nat. Commun.* **13**, 1–12 (2022).
- Young, I. R., Zieger, S. & Babanin, A. V. Global trends in wind speed and wave height. *Science (1979)* **332**, 451–455 (2011).
- Nicholls, R. J. et al. A global analysis of subsidence, relative sea-level change and coastal flood exposure. *Nat. Clim. Change* **11**, 338–342 (2021).
- Lansu, E. M. et al. A global analysis of how human infrastructure squeezes sandy coasts. *Nat. Commun.* **15**, 1–7 (2024).
- Liu, C., Liang, X., Ponte, R. M., Vinogradova, N. & Wang, O. Vertical redistribution of salt and layered changes in global ocean salinity. *Nat. Commun.* **10**, 1–8 (2019).
- Allan, H., Levin, N. & Kark, S. Quantifying and mapping the human footprint across Earth's coastal areas. *Ocean Coast. Manag.* **236**, 106476 (2023).
- Halpern, B. S. et al. A global map of human impact on marine ecosystems. *Science (1979)* **319**, 948–952 (2008).
- Wei, J. et al. Global estimation of suspended particulate matter from satellite ocean color imagery. *J. Geophys. Res. Oceans* **126**, e2021JC017303 (2021).
- Cao, Z. et al. What water color parameters could be mapped using MODIS land reflectance products: A global evaluation over coastal and inland waters. *Earth Sci. Rev.* **232**, 104154 (2022).
- Qiu, L., He, J., Yue, C., Ciais, P. & Zheng, C. Substantial terrestrial carbon emissions from global expansion of impervious surface area. *Nat. Commun.* **15**, 1–13 (2024).
- Li, J. et al. Recent intensified erosion and massive sediment deposition in Tibetan Plateau rivers. *Nat. Commun.* **15**, 1–12 (2024).
- Lyne, V. D., Butman, B. & Grant, W. D. Sediment movement along the U.S. east coast continental shelf—II. Modelling suspended sediment concentration and transport rate during storms. *Cont. Shelf Res.* **10**, 429–460 (1990).
- Stroud, J. R. et al. Assimilation of satellite images into a sediment transport model of Lake Michigan. *Water Resour. Res.* **45**, 2419 (2009).
- Sun, X. et al. Changes in global fluvial sediment concentrations and fluxes between 1985 and 2020. *Nat. Sustain.* 1–10 <https://doi.org/10.1038/s41893-024-01476-7> (2025).
- Cao, Z. et al. MODIS observations reveal decrease in lake suspended particulate matter across China over the past two decades. *Remote Sens. Environ.* **295**, 113724 (2023).
- Yu, X. et al. An empirical algorithm to seamlessly retrieve the concentration of suspended particulate matter from water color across ocean to turbid river mouths. *Remote Sens. Environ.* **235**, 111491 (2019).
- Wilson, R. J. & Heath, M. R. Increasing turbidity in the North Sea during the 20th century due to changing wave climate. *Ocean Sci.* **15**, 1615–1625 (2019).
- Bramante, J. F., Ashton, A. D., Storlazzi, C. D., Cheriton, O. M. & Donnelly, J. P. Sea level rise will drive divergent sediment transport patterns on fore reefs and reef flats, potentially causing erosion on Atoll Islands. *J. Geophys. Res. Earth Surf.* **125**, e2019JF005446 (2020).
- Syvitski, J. et al. Earth's sediment cycle during the anthropocene. *Nat. Rev. Earth Environ.* **3**, 179–196 (2022).
- Dethier, E. N., Renshaw, C. E. & Magilligan, F. J. Rapid changes to global river suspended sediment flux by humans. *Science (1979)* **376**, 1447–1452 (2022).
- Hou, X., Xie, D., Feng, L., Shen, F. & Nienhuis, J. H. Sustained increase in suspended sediments near global river deltas over the past two decades. *Nat. Commun.* **15**, 1–12 (2024).
- Paolo, F. et al. Satellite mapping reveals extensive industrial activity at sea. *Nature* **625**, 85–91 (2024).
- Qiu, Z. et al. Using Landsat 8 data to estimate suspended particulate matter in the Yellow River estuary. *J. Geophys. Res. Oceans* **122**, 276–290 (2017).
- Zhao, G., Jiang, W., Wang, T., Chen, S. & Bian, C. Decadal variation and regulation mechanisms of the suspended sediment concentration in the Bohai Sea, China. *J. Geophys. Res. Oceans* **127**, e2021JC017699 (2022).

34. Stachowska, Z., van der Bilt, W. G. M. & Strzelecki, M. C. Coastal lake sediments from Arctic Svalbard suggest colder summers are stormier. *Nat. Commun.* **15**, 9688 (2024).
35. Feng, D. et al. Drivers and impacts of sediment deposition in Amazonian floodplains. *Nat. Commun.* **16**, 1–12 (2025).
36. Nienhuis, J. H. et al. Global-scale human impact on delta morphology has led to net land area gain. *Nature* **577**, 514–518 (2020).
37. Wang, S. et al. Reduced sediment transport in the Yellow River due to anthropogenic changes. *Nat. Geosci.* **9**, 38–41 (2015).
38. Liu, Z., Fagherazzi, S. & Cui, B. Success of coastal wetlands restoration is driven by sediment availability. *Commun. Earth Environ.* **2**, 1–9 (2021).
39. Wang, S. et al. Trophic state assessment of global inland waters using a MODIS-derived Forel-Ule index. *Remote Sens. Environ.* **217**, 444–460 (2018).
40. Sayre, R. et al. A new map of global islands. *researchgate.net* (2019).
41. Chen, T. & Guestrin, C. XGBoost: a scalable tree boosting system. In *Proc. ACM SIGKDD International Conference on Knowledge Discovery and Data Mining* 785–794 (ACM, 2016).
42. Petus, C. et al. Estimating turbidity and total suspended matter in the Adour River plume (South Bay of Biscay) using MODIS 250-m imagery. *Elsevier* **30**, 379–392 (2010).
43. Balasubramanian, S. V. et al. Robust algorithm for estimating total suspended solids (TSS) in inland and nearshore coastal waters. *Remote Sens. Environ.* **246**, 111768 (2020).
44. Waga, H., Eicken, H., Light, B. & Fukamachi, Y. A neural network-based method for satellite-based mapping of sediment-laden sea ice in the Arctic. *Remote Sens. Environ.* **270**, 112861 (2022).
45. Zhang, X. et al. Determining the drivers of suspended sediment dynamics in tidal marsh-influenced estuaries using high-resolution ocean color remote sensing. *Remote Sens. Environ.* **240**, 111682 (2020).
46. Hu, C. et al. Dynamic range and sensitivity requirements of satellite ocean color sensors: learning from the past. *opg.optica.org* C Hu, L Feng, Z Lee, CO Davis, A Mannino, CR McClain, BA Franz *Applied Optics*, 2012•*opg.optica.org*.
47. Chen, H., Covert, I. C., Lundberg, S. M. & Lee, S. I. Algorithms to estimate Shapley value feature attributions. *Nat. Mach. Intell.* **5**, 590–601 (2023).
48. Global coastal water clarity has increased due to human intervention. https://figshare.com/articles/dataset/Global_coastal_water_clarity_has_increased_due_to_human_intervention/29581982.

Acknowledgements

We would like to thank Google Earth Engine (GEE) for providing long-term remote sensing data, Hao Yu and Jiasheng Tang for their contributions to the discussion, and Ze Yuan and Zilong Xia for their help in early code writing. This work is supported by the Strategic Priority Research Program of Chinese Academy of Sciences (Grant No. XDB0740300), the National Natural Science Foundation of China (No. 42476195), the Youth Innovation Promotion Association of Chinese Academy of Sciences (2023060) and the Jiangsu Provincial Government Overseas Talent 100 Plan (SBX2021010183).

Author contributions

Fengqin Yan contributed to the conceptualization, methodology design, data analysis, and manuscript drafting. Bin He led the project, coordinated

research activities, and contributed to data interpretation and manuscript preparation. Vincent Lyne provided valuable input on refining the manuscript structure and improving the clarity of the text. Rong Fan contributed to the development of analytical tools and conducted key computational experiments. Yikun Cui assisted with the validation of satellite-derived results and provided technical guidance. Xinyi Wang performed data visualization and supported the preparation of Supplementary Materials. Dongjie Fu contributed to the statistical analysis and participated in data curation. Michael Meadows offered insights into coastal ecosystem processes and provided critical feedback on the manuscript. John Wilson contributed to the interpretation of environmental shifts and the broader implications of the findings. Ziyang Chen enhanced the quality and presentation of the figures included in the manuscript. Chengyuan Ju assisted in coordinating international collaborations and contributed to manuscript revisions. Fenzhen Su led the project by supervising the research, securing funding, and providing strategic guidance throughout the study, including support in finalizing the manuscript for submission.

Competing interests

The authors declare no competing interests.

Additional information

Supplementary information The online version contains supplementary material available at <https://doi.org/10.1038/s43247-025-02638-x>.

Correspondence and requests for materials should be addressed to Fenzhen Su.

Peer review information *Communications Earth and Environment* thanks Emily Douglas and the other anonymous reviewer(s) for their contribution to the peer review of this work. Primary handling editors: Olusegun Dada and Alice Drinkwater. [A peer review file is available].

Reprints and permissions information is available at <http://www.nature.com/reprints>

Publisher's note Springer Nature remains neutral with regard to jurisdictional claims in published maps and institutional affiliations.

Open Access This article is licensed under a Creative Commons Attribution-NonCommercial-NoDerivatives 4.0 International License, which permits any non-commercial use, sharing, distribution and reproduction in any medium or format, as long as you give appropriate credit to the original author(s) and the source, provide a link to the Creative Commons licence, and indicate if you modified the licensed material. You do not have permission under this licence to share adapted material derived from this article or parts of it. The images or other third party material in this article are included in the article's Creative Commons licence, unless indicated otherwise in a credit line to the material. If material is not included in the article's Creative Commons licence and your intended use is not permitted by statutory regulation or exceeds the permitted use, you will need to obtain permission directly from the copyright holder. To view a copy of this licence, visit <http://creativecommons.org/licenses/by-nc-nd/4.0/>.

© The Author(s) 2025, corrected publication 2025